Int. J. Electrochem. Sci., 14 **(2019)** 7673 – 7683, doi: 10.20964/2019.08.11

International Journal of
ELECTROCHEMICAL
SCIENCE
www.electrochemsci.org

Short Communication

Novel fabrication of $Li_4Ti_5O_{12}$ coated $LiMn_2O_4$ nanorods as cathode materials with long-term cyclic stability at high ambient temperature

Chengyi Zhu[1], *Jianxiong Liu*[1], *Xiaohua Yu*[1], *Yingjie Zhang*[1,2], *Xiaodong Jiang*[1], *Peng Dong*[2,*], *Yannan Zhang*[2,*]

[1] Faculty of Materials Science and Engineering, Kunming University of Science and Technology, Kunming 650093, China
[2] National and Local Joint Engineering Laboratory for Lithium-ion Batteries and Materials Preparation Technology, Key Laboratory of Advanced Battery Materials of Yunnan Province, Faculty of Metallurgical and Energy Engineering, Kunming University of Science and Technology, Kunming 650093, China
[*]E-mail: dongpeng2001@126.com (Peng Dong), zyn_legolas@163.com (Yannan Zhang)

Received: 7 April 2019 / *Accepted:* 15 May 2019 / *Published:* 30 June 2019

Spinel $LiMn_2O_4$ has attracted increasing interest as promising cathode material owing to its low cost, high safety, and environmental friendliness. But the further development of $LiMn_2O_4$ is restricted by fast capacity fading upon cycling, especially at high temperatures. Herein, the one-dimensional (1D) $Li_4Ti_5O_{12}$ coated $LiMn_2O_4$ nanorods (LMO-LTO) are successfully prepared by combining sol-gel and solid-state calcination method and ultimately enhance the cathode utilization in high-temperature and long-cycling conditions. The as-prepared LMO-LTO cathode delivers a high initial discharge capacity of 128.5 mAh g^{-1} at 0.1 C rate and exhibits a promising discharge capacity over 74.5 mAh g^{-1} at 10 C rate. Even under an elevated temperature of 55°C, it still maintains 74.8% of its initial capacity at 1 C rate. Furthermore, the electrochemical impedance spectra (EIS) measurement confirm that compared with the pure $LiMn_2O_4$ nanorod, lower the charge transfer resistance (R_{ct}) and enhanced Li^+ diffusion coefficient are also strong evidences of the improved electrochemical performance of $LiMn_2O_4$ nanorods after $Li_4Ti_5O_{12}$ coating.

Keywords: Lithium-ion batteries; $LiMn_2O_4$ nanorods; $Li_4Ti_5O_{12}$ coating; High ambient temperature

1. INTRODUCTION

Spinel $LiMn_2O_4$ has been recognized as one of the most promising cathodes for advanced lithium-ion batteries (LIBs) and promising energy-storage systems for applications in electric vehicles,

hybrid vehicles, and portable devices owing to its nontoxicity, high safety property, and abundant manganese resource [1-3]. However, the successful commercialization of $LiMn_2O_4$ is restricted owing to rapid capacity fading upon cycling process, especially high ambient temperature. The performance deterioration of $LiMn_2O_4$ electrode mainly origins from unremarkable lithium diffusion kinetics and the dissolution of manganese in the electrolyte containing $LiPF_6$ salt and carbonate solvent [4-6]. To resolve the former issues, the design and tailoring to generate specific shape and sizes of nanomaterials have become one of the research hotspots [7-8]. Noticeably, one-dimensional (1D) materials are particularly attractive since they can provide a short path for Li^+ transport [9]. However, although one-dimensional $LiMn_2O_4$ can facilitate the transport of Li ions and improve the capacity density of $LiMn_2O_4$ effectively, the capacity fading after long-term cycling at elevated temperature is not addressed.

Surface modification is an effective way to suppress the manganese dissolution. The materials such as Al_2O_3 [10], AlF_3 [11], V_2O_5 [12], TiO_2 [13] have been reported to prevent the $LiMn_2O_4$ cathode and improve cyclic stability. However, the majority of these coating materials usually have a negative impact on the initial capacity of cathode materials. Spinel $Li_4Ti_5O_{12}$ is considered to be an effect coating mater to improve both initial discharge capacity and cyclic stability. Wu et al. [14] prepared $Li_4Ti_5O_{12}$ coated $LiNi_{0.5}Mn_{1.5}O_4$ via a hydrothermal method, and compare to the pure $LiNi_{0.5}Mn_{1.5}O_4$, the as-prepared $LiNi_{0.5}Mn_{1.5}O_4$@$Li_4Ti_5O_{12}$ exhibited an improved specific capacity of 141.2 mAh g^{-1} at 0.2 C and maintained a capacity retention of 97.03% after 140 cycles at 1 C under 55℃.

In this work, we have successfully fabricated $Li_4Ti_5O_{12}$ coated $LiMn_2O_4$ nanorods as cathode materials by combining sol-gel and solid-state calcination method. The as-prepared sample delivers superior long-cycling performance and excellent rate ability, which can be associated with the suppression of the manganese dissolution.

2. EXPERRIMENTAL METHODS

2.1 Synthesis of β-MnO_2 nanorods

The *β*-MnO_2 nanorods were successfully synthesized through a hydrothermal method. Firstly, 3.0 g $KMnO_4$ (Shanghai Aladdin Reagent, 99.9%) and 10 mL ethanol were fully dissolved in 120 mL deionized water with vigorously stirring. After that, the obtained mixed solution was transferred into a 150 mL Teflon-lined stainless-steel autoclave and reacted at 160℃ for 15 hours. The precursor was collected after washing and filtering for three times, followed by drying at100°C in a vacuum oven for 10 h. Finally, the *β*-MnO_2 nanorods were obtained after calcining at 350℃ for 1.5 hours under air flow.

2.2 Synthesis of $LiMn_2O_4$ nanorods

$LiMn_2O_4$ nanorods were prepared via a solid-state reaction route using as-prepared *β*-MnO_2 as self-sacrifice precursors. Typically, stoichiometric amounts of $LiOH{\cdot}H_2O$ (Shanghai Aladdin Reagent, 99.9%), *β*-MnO_2 nanorods were fully dispersed by deionized water with strong mechanical stirring for 2 h. Subsequently, the solvent was evaporated at 100°C for 3 h in a vacuum oven. Finally, the obtained powder was sintered at 700 °C for 10 h to obtain the $LiMn_2O_4$ nanorods.

2.3 Synthesis of $Li_4Ti_5O_{12}$ coated $LiMn_2O_4$ nanorods

$Li_4Ti_5O_{12}$ coated $LiMn_2O_4$ nanorods were synthesized by a modified sol-gel method to control the hydrolysis and condensation of titanium tetrabutoxide (TBOT, Shanghai Aladdin Reagent, 99.9%) in ethanol/ammonia mixtures. Typically, the as-prepared pristine $LiMn_2O_4$ nanorods and 3 mL ammonia were added in 100 mL absolute ethanol. Meanwhile, 0.6 mL of TBOT was slowly added with strong magnetic stirring. After stirring for 4 h, the resultant products were centrifuged and washed several times and then dried at 80°C in a vacuum oven for 12 h. After that, the obtained particles and 0.1 g $LiOH·H_2O$ were mixed together and calcined at 600°C for 10 h under air flow to obtain $Li_4Ti_5O_{12}$-coated $LiMn_2O_4$ nanorods.

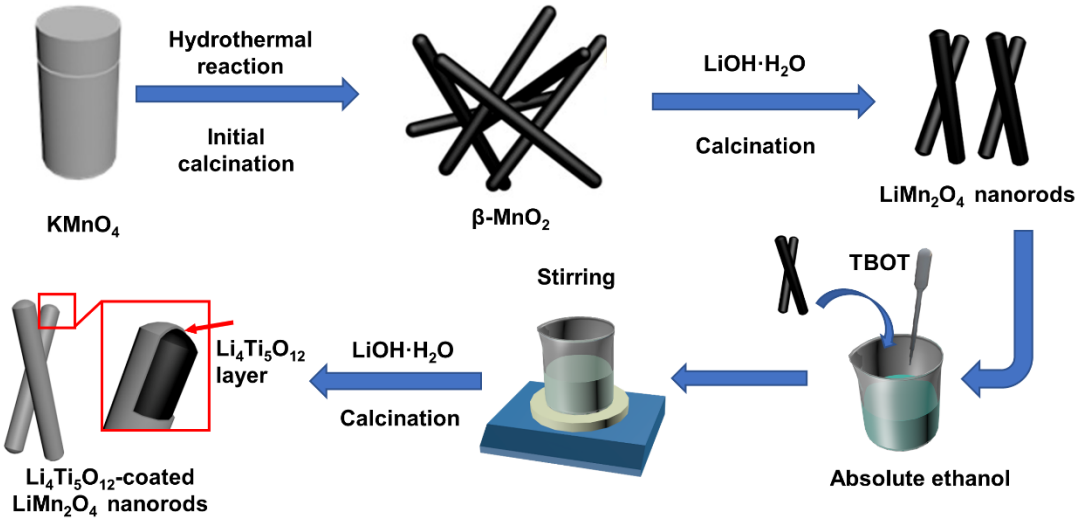

Figure 1. Flowchart for the preparation of $LiLa_xMn_{2-x}O_4$ nanorods.

2.4 Material characterization

The crystalline structures of the obtained $LiLa_xMn_{2-x}O_4$ (x=0, 0.01, 0.03, 0.05 & 0.10) nanorods were accomplished on X-ray diffraction (XRD, D/MAX-2500 X) using Cu Kα radiation (λ = 1.5406 Å) in the 2θ range from 10°-85°. Raman spectra were performed with a Jobin-Yvon model U1000 with a wavelength of 512.3 nm. The surface chemical valence of the samples was taken by X-ray photoelectron spectroscopy (XPS, PHI5600). The surface morphologies and crystalline microstructures of samples were observed by field emission scanning electron microscope (FESEM, Zeiss Supra 55VP) and transmission electron microscopy (TEM, FEI Tecnai F20). The element distribution was confirmed by energy dispersive spectrometer (EDS, PHI5000 Versa probe-II). The amounts of manganese dissolution were carried out by inductively coupled plasma emission spectrograph (ICP, Thermo-6000).

The coin cell preparation and detailed electrochemical analysis procedures were following our previous reports [15]. To evaluate the electrochemical performance, cyclic charge/discharge curves were performed at various current densities in a voltage window of 3.0 V and 4.5 V on a battery test system (BTS, Neware, China). The electrochemical impedance spectra (EIS) was conducted using an

electrochemical workstation (CHI760E, Chenhua) ranging from 1 mHz to 1 MHz with an amplitude of 5 mV.

3. RESULTS AND DISCUSSION

The crystalline structure and phase purity of LMO and LMO-LTO samples are detected by XRD patterns, as shown in Figure. 2a. Both of the as-prepared samples can be identified as well-defined spinel structure of $LiMn_2O_4$ with the F*d3m* space group (JCPDS 35-0782) and no impurity peaks appeared, indicating that the heat treatment in the coating route does not induce a structural transformation of spinel $LiMn_2O_4$ [16]. To further explain the influence of $Li_4Ti_5O_{12}$ coating, the enlarged peaks of (111) are exhibited in Figure. 2b, it can be clearly observed that the position of the (111) peak shifts to a negative degree, which indicates the increase of lattice parameter after $Li_4Ti_5O_{12}$ coating. The increase of lattice constant may be because that some of the Mn^{4+} ions with the smaller radius (r＝0.053 nm) in $LiMn_2O_4$ are replaced by Ti^{4+} ions (r=0.061 nm) [17].

The Raman spectra of LMO and LMO-LTO are shown in Figure. 2c. As can be seen from the figure, $A_{1g} + E_g + 3F_{2g}$ are Raman active modes for the spinel structure of $LiMn_2O_4$ [18]. All the Raman scattering spectrum of as-prepared samples are dominated by a strong and broad-band at around 620 cm^{-1} with a shoulder at around 580 cm^{-1}, which correspond to the A_{1g} and $F_{2g}^{(1)}$ symmetry, respectively. A band with a medium intensity appears at around 485 cm^{-1} and can be assigned to the $F_{2g}^{(2)}$ symmetry. Two low wavenumber bands are observed at around 387 and 301 $cm^{-1}$and can be attributed to the E_g and $F_{2g}^{(3)}$ symmetry, respectively. Compared with the pristine one, a slight decrease in peak intensity of LMO-LTO can be observed, indicating that the coating layer affects the scattering signal from $LiMn_2O_4$ in the experiment [19].

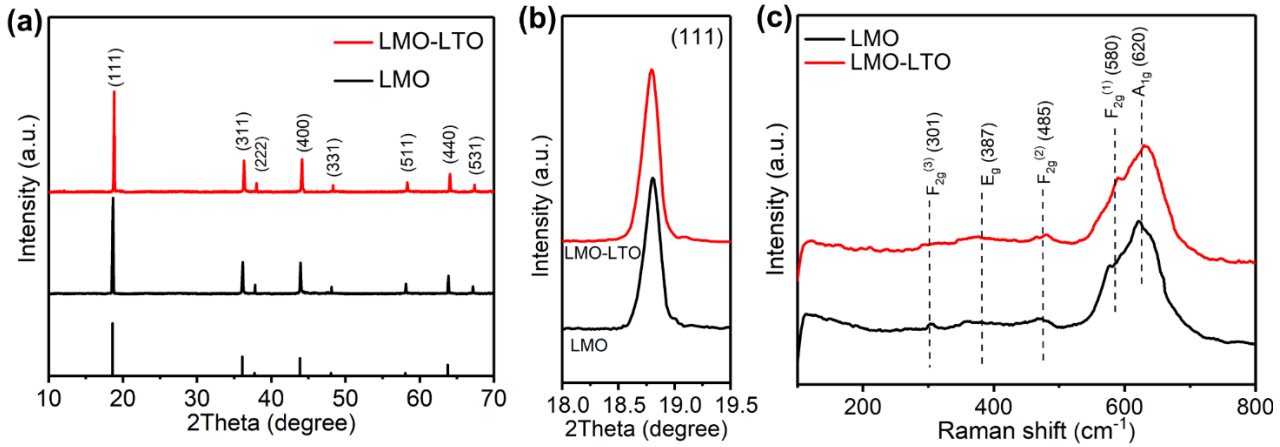

Figure 2. The XRD patterns of LMO and LMO-LTO (a) and the enlarged peak of (111) (b); Raman scattering spectrum of as-prepared samples (c).

In order to analyze the surface compositions of the as-prepared samples, Figure. 3a shows the XPS full spectra of LMO and LMO-LTO samples. Compared with the spectrum of LMO-0, besides the main peaks of Mn 2p, O 1s, C 1s, and Li 1s, two characteristic peaks at 458.3 eV and 464.2 eV attributed

to Ti $2p_{1/2}$ and Ti $2p_{3/2}$ peaks of Ti^{4+} in the spectrum of LMO-LTO (Figure. 3b) [20]. In order to further explain the valence state change of Mn element after $Li_4Ti_5O_{12}$ coating, the high-resolution spectra for Mn 2p of LMO and LMO-LTO are illustrated in Figure. 3c and d, respectively. The peaks at 642.1 and 643.4 eV of the Mn $2p_{3/2}$ spectrum are assigned to Mn^{3+} and Mn^{4+}, which illustrates that the Mn oxidation state in $LiMn_2O_4$ nanorod is between +3 and +4 [21]. Additionally, the Mn^{3+}/Mn^{4+} contents of LMO and LMO-LTO samples estimated by the peak area of Mn $2p_{3/2}$ and Mn $2p_{3/2}$ are 50.4%/49.6% and 48.3%/51.7%, respectively. Obviously, Mn^{3+} concentration is gradually increased after $Li_4Ti_5O_{12}$ coating. This result is consistent well with the information obtained from XRD patterns.

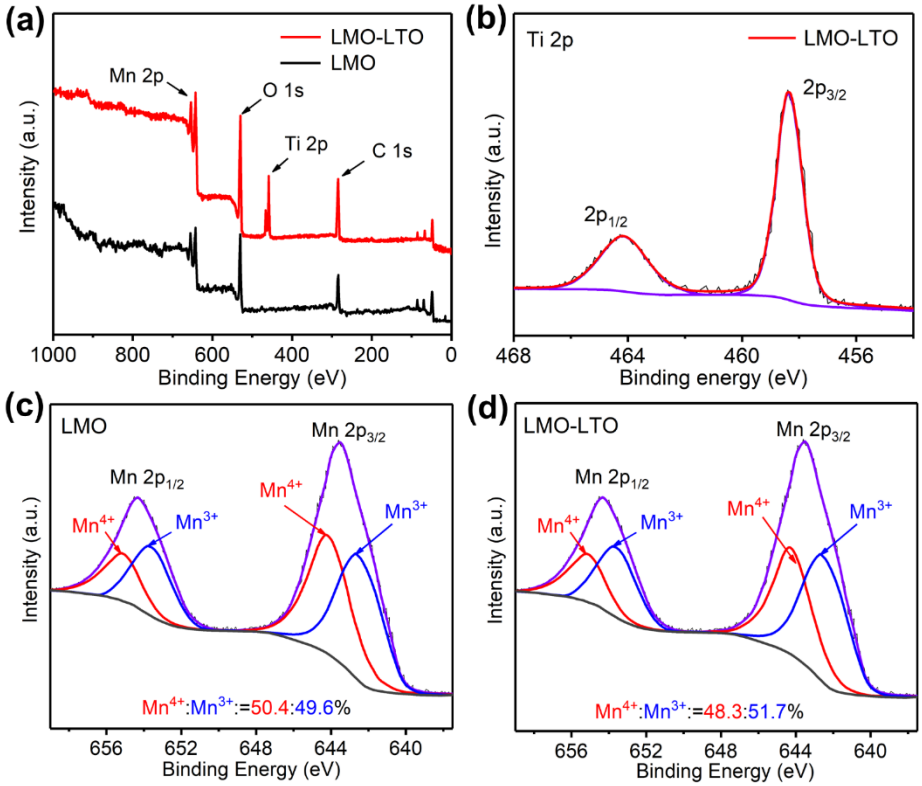

Figure 3. XPS full spectra of LMO and LMO-LTO samples (a); High-resolution spectra for Ti 2p of LMO-LTO sample (b); High-resolution spectra for Mn 2p of LMO (C) and LMO-LTO samples (d).

Figure. 4a exhibits the SEM image of the resulting β-MnO_2. It can be observed that the obtained β-MnO_2 product consists mainly of nanorods with an average diameter of 60 nm. Figure. 4b and c show the LMO and LMO-LTO samples, respectively. Both of the samples deliver a well-defined rod-like morphology with an average diameter of 100 nm. Compared to the LMO sample, after surface modification of $Li_4Ti_5O_{12}$, it is not difficult to observe a rougher coating layer on the surface of LMO-LTO sample. What' more, the EDS mappings of the LMO-LTO are shown in Figure. 4d, it can be clearly seen that Mn, O, and Ti elements are homogeneously distributed, implying that the $Li_4Ti_5O_{12}$ have been successfully coated on the surface of $LiMn_2O_4$ nanorods. In order to further confirm the presence of the $Li_4Ti_5O_{12}$ coating layer, the TEM images of as-prepared samples are shown in Figure. 4e and f,

respectively. Consistent with SEM results, both samples exhibit the rod-like structures and grow along the (111) crystal plane. Obviously, LMO-LTO sample is covered with $Li_4Ti_5O_{12}$ coating layer with a approximately thickness of approximately 12 nm.

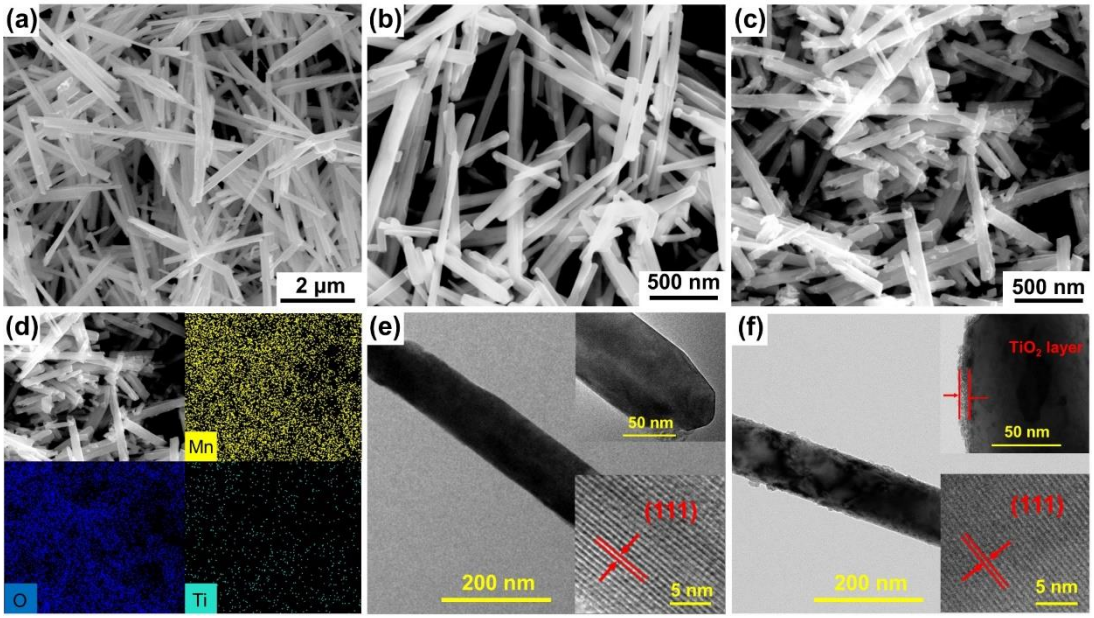

Figure 4. SEM imagines of β-MnO2 nanorods (a), LMO (b) and LMO-LTO (c); EDS mapping images of LMO-LTO (d); TEM images of LMO (e) and LMO-LTO (f).

To evaluate the effect of deformation on the electrochemical properties of bare and $Li_4Ti_5O_{12}$ coated electrodes, the electrodes were tested by galvanostatic measurements at a voltage of 3.0-4.5 V. The initial charge/discharge curves of LMO and LMO-LTO at 0.1 C rate are shown in Figure. 5a. Both of the samples deliver two plateaus around 4.1 V and 3.9 V, respectively, which correspond to the chemical reactions of equation (1) and equation (2) [22]:

$$MnO_2 + 0.5Li^+ + 0.5e^- = Li_{0.5}Mn_2O_4 \quad (1)$$

$$Li_{0.5}Mn_2O_4 + 0.5Li^+ + 0.5e^- = LiMn_2O_4 \quad (2)$$

What' more, the initial discharge capacity of LMO is 122.5 mAh g^{-1}, while LMO-LTO delivers a higher capacity than the pristine one (128.5 mAh g^{-1}). The increased specific capacity after $Li_4Ti_5O_{12}$ coating can be associated with the decreased average Mn valence (<3.5) and the suppression of side reactions between the cathode and electrolyte during the first charge/discharge process [23]. The rate performance of as-prepared samples at various current density are carried out and shown in Figure. 5b. With the increase of current density, compared with LMO, LMO-LTO exhibits significantly improved capacity, even at a high current density of 10 C, the discharge capacity of it can still remain up to 74.5 mAh g^{-1}. In addition, the discharge capacity of LMO-LTO can be recovered to its initial value when the current density returns to 0.1 C, indicating that LMO-LTO samples have good electrochemical reversibility and structural stability.

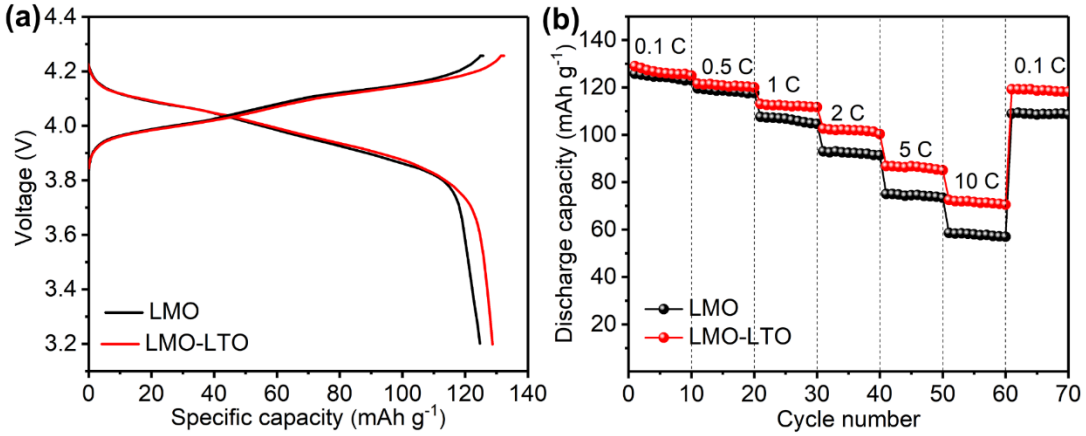

Figure 5. The initial charge/discharge curves of LMO and LMO-LTO at 0.1 C rate (a); the rate performance of LMO and LMO-LTO at different current density (b).

In order to evaluate the cycle life of $LiMn_2O_4$ nanorods before and after coating, a series of long-term cycles for LMO and LMO-LTO electrodes are tested under both normal and high ambient temperature. Figure. 6a presents the cycle stability test results of as-prepared samples at 1 C under 25℃. The reversible capacity of LMO-LTO remains at 98.4 mAh g^{-1} with an excellent capacity retention of 82.2% after 500 cycles at 1 C. For comparison, the discharge capacity of the pure LMO sample decreases from 118.1 mAh g^{-1} to 64.3 mAh g^{-1} with a capacity retention of 54.5%. Figure. 6b exhibits the cyclic performance of LMO and LMO-LTO cathodes at 1 C under 55℃, respectively. Both of the samples display declined capacities at elevated temperature, which may due to the accelerated Mn dissolution in the electrolyte. The discharge capacity of LMO sharply fades to 38.6 mAh g^{-1} after 500 cycles, while LMO-LTO only decreases to 89.2 mAh g^{-1} with a capacity retention of 74.8%.

In addition, we compared the cycle performance of LMO-LTO cathode with some previous reports of surface-modified $LiMn_2O_4$ cathodes and the relevant data are shown in the Table 1. It is noted that even after 500 cycles, the as-prepared LMO-LTO cathode still exhibits excellent capacity retention under both normal and high ambient temperature. The superior cyclic stability of LMO-LTO can be attributed to the suppression of manganese dissolution after $Li_4Ti_5O_{12}$ coating [24]. In order to confirm this standpoint, the amounts of Mn dissolution for LMO and LMO-LTO are examined by ICP measurement after 3 weeks of storage in $LiPF_6$/EC: DEC (1:1) electrolyte at 25℃ and 55℃, respectively, as shown in Figure. 6c. Compared to LMO, LMO-LTO exhibits a significant reduction of Mn dissolved amount at both normal and high ambient temperature. On the basis of ICP measurement, it can be concluded that the $Li_4Ti_5O_{12}$ coating layer can significantly suppress the manganese dissolution and prolong the cycle life.

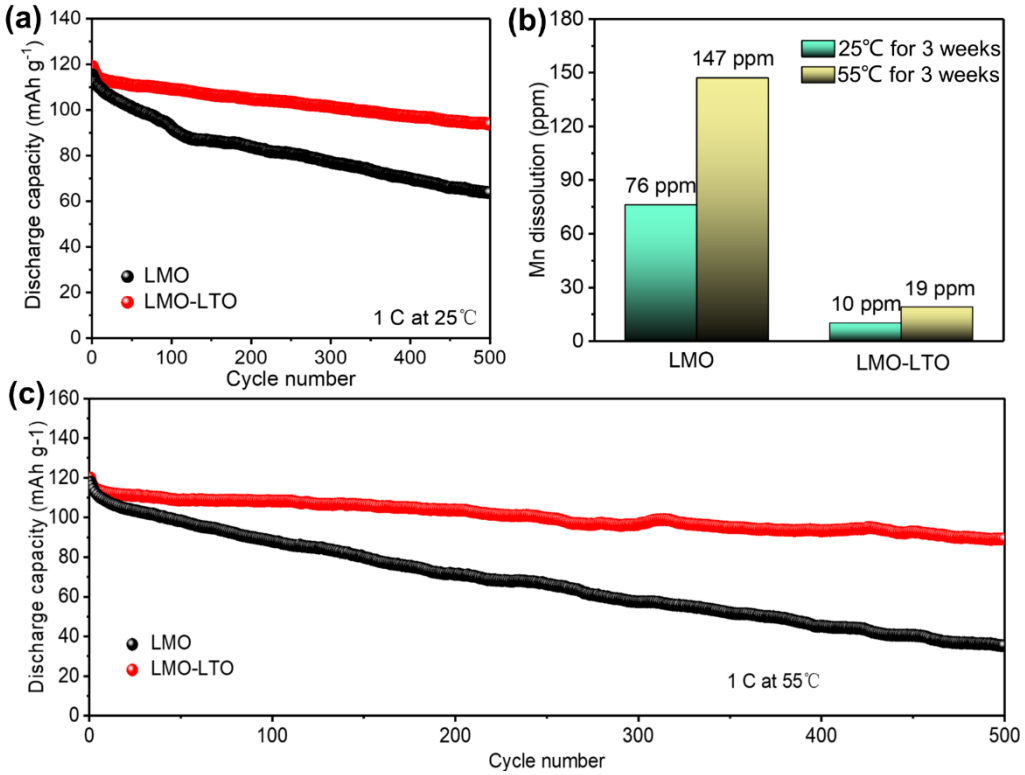

Figure 6. Cycling performances at 25℃ (a) and 55℃ (b) of LMO and LMO-LTO nanorods; Concentration of Mn dissolved from LMO-0 and LMO-3 samples stored in $LiPF_6$/EC: DEC (1:1) electrolyte at 25℃ and 55℃ for 30 days (c).

Table 1. The comparison for the cycling performance with some previous reports of surface-modified $LiMn_2O_4$ cathodes

Coating materials	Discharge capacity and capacity retention after several cycles at certain rate	
	25ºC	55ºC
$Li_4Ti_5O_{12}$ (our work)	98.4 mAh g^{-1},82.2%, 500 cycles, 1 C	89.2 mAh g^{-1},74.8%, 500 cycles, 1 C
TiO_2 [13]	113 mAh g^{-1},90.1%, 250 cycles, 0.2 C	77.1 mAh g^{-1},62.2%, 250 cycles, 0.2 C
SiO_2 [25]	101.7 mAh g^{-1},97.6%, 100 cycles, 1 C	93 mAh g^{-1},88.7%, 100 cycles, 1 C
YPO_4 [26]	90 mAh g^{-1},84.1%, 100 cycles, 0.2 C	86.1 mAh g^{-1},80.3%, 100 cycles, 0.2 C
Al_2O_3 [27]	109 mAh g^{-1},99.0%, 100 cycles, 1 C	77.2 mAh g^{-1},67.5%, 100 cycles, 1 C
Nano-TiO2(B) [28]	-	77.4 mAh g^{-1},73.7%, 300 cycles, 0.5 C

The electrochemical impedance spectra (EIS) measurement were carried out to study the insertion and de-intercalation mechanism of Li^+ at the electrode/electrolyte interface. Figure. 7a and b exhibit the Nyquist plots of LMO and LMO-LTO electrodes measured during the first discharge and

after 100 cycles, respectively. All the as-prepared samples exhibit typical Nyquist plots, including the depressed semicircles and the oblique lines. The intercept represents the solution resistance (R_s), while the semicircle reflects the charge transfer resistance (R_{ct}) [29]. the results of R_s and R_{ct} values were fitted using the equivalent circuit (the inset of Figure 7) and listed in Table 1. In addition, the Li^+ diffusion coefficient of as-prepared samples can be obtained from the following equations [30]:

$$Z' = R_s + R_{ct} + \sigma_\omega \cdot \omega^{-0.5} \quad (3)$$

$$D_{L_i} = \frac{R^2T^2}{2A^2F^4\sigma_\omega^2C^2} \quad (4)$$

where R represents the gas constant (8.314 $JK^{-1}mol^{-1}$), A is the efficient work area of the electrode (1.74 cm^2), F is the Faraday's constant (96485.3 C/mol), σ_ω represents the Warburg impedance coefficient and T represents the absolute temperature (298 K) [31]. The diffusion coefficient (D_{Li}) of LMO and LMO-LTO samples calculated from the equation (3) and (4) are listed in Table 1. Both of the samples have similar D_{Li} before cycling, indicating that the $Li_4Ti_5O_{12}$ coating does not hinder the diffusion of lithium ions. Differently, after 100 cycles, LMO-LTO electrode has a low D_{Li} value of 1.02×10^{-13} cm^2s^{-1} compared to the bare electrode (5.22×10^{-13} cm^2s^{-1}). It may because that the $Li_4Ti_5O_{12}$ coating layer can effectively suppress continuous growth of solid electrolyte interface (SEI) film and enhance the Li^+ diffusion transportation [32]. The enhanced Li^+ diffusion coefficient after $Li_4Ti_5O_{12}$ coating contributes significantly to the excellent rate performance and cyclic stability of the $LiMn_2O_4$ nanorods.

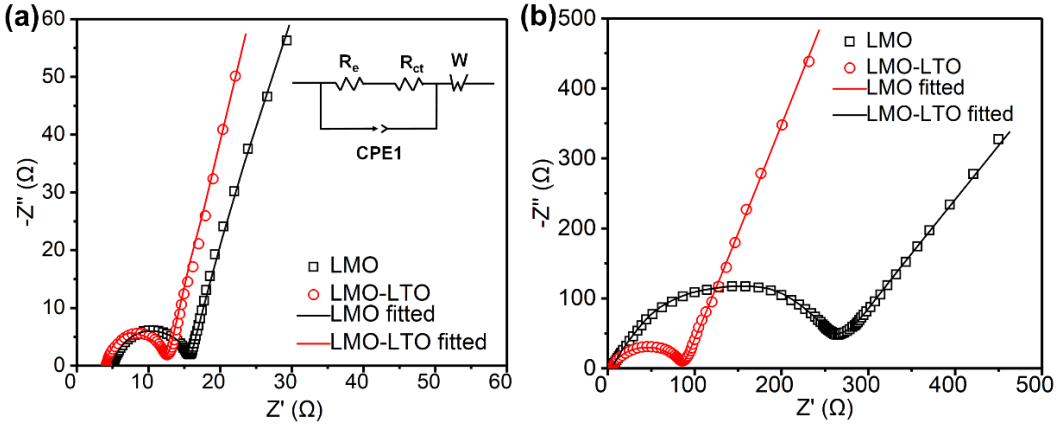

Figure 7. Impedance spectra (Nyquist plots) of LMO and LMO-LTO before cycling (a) and after 100 cycles at 25°C (b). The scatter points are the experimental data and the lines represent the simulation results using the equivalent circuit shown in the inset of (a).

Table 2. R_s, R_{ct}, σ and D_{Li} values for LMO and LMO-LTO samples

Sample	R_s/Ω	R_{ct}/Ω	$\sigma/(\Omega/s^{1/2})$	$D_{Li}/(cm^2s^{-1})$
Before cycling				
LMO	5.24	8.45	12.6	4.78×10^{-12}
LMO-LTO	4.33	6.58	13.9	5.33×10^{-12}

After 100 cycles				
LMO	12.68	156.27	34.7	5.22×10^{-13}
LMO-LTO	6.54	54.2	16.4	1.02×10^{-13}

4. CONCLUSION

In this work, $Li_4Ti_5O_{12}$ coated $LiMn_2O_4$ nanorods (LMO-LTO) were successfully fabricated by combining sol-gel and solid-state calcination method. The structure and morphology measurements show that the as-prepared sample displays the unique rod-like morphology with a continuous and uniform coating layer. LMO-LTO cathode exhibits the initial capacity of 128.5 mAh g^{-1} and prolonged capacity retention (74.8% of its initial capacity) after 500 cycles at 55℃. The enhanced rate capacity and excellent long-term cycling performance under high ambient temperature could be attributed to the suppression of manganese dissolution after $Li_4Ti_5O_{12}$-coating. Furthermore, the $Li_4Ti_5O_{12}$ coating layer can decrease the byproducts covered on the electrode surface, thus cutting down the interface impedance and enhancing the kinetics of the Li^+ diffusion. The technology introduced herein offers an effective strategy to enable the use of spinel-based cathode materials.

ACKNOWLEDGEMENTS
Financial support from National Natural Science Foundation of China (No. 51764029, 51665022, and 51601081) and Yunnan Natural Science Foundation (No. 2018FB087) are gratefully acknowledged.

References

1. M. Li, J. Lu, Z. W. Chen and K. Amine, *Adv. Mater*., 30 (2018) 1800561.
2. Y. N. Zhang, Y. Y. Zhang, Y. J. Zhang, P. Dong, Q. Meng and M. L. Xu, *J. Alloy. Compd*., 783 (2019) 357.
3. S. L. Luo, H. J. Guo, S.K. Zhang, Z. X. Wang, X. H. Li, G. C. Yan and J. X. Wang, *Ceram. Int.*, 45 (2019) 8607.
4. C. Zhan, T. P. Wu, J. Lu and K. Amine, *Energy Environ. Sci.,* 11 (2018) 243.
5. L. B. Ben, H. L. Yu, B. Chen, Y. Y. Chen, Y. Gong, X. N. Yang, L. Gu and X. J. Huang, *ACS Appl. Mater. Interfaces*, 9 (2017) 35463.
6. Y. L. Qiao, Z. Zhou, Z. X. Chen, S. C. Du, Q. Cheng, H. W. Zhai, N. J. Fritz, Q. Du and Y. Yang, *Nano Energy*, 45 (2018) 68.
7. A. G. Kashkooli, E. Foreman, S. Farhad, D. U. Lee, W. Ahn, K. Feng, V. D. Andrade and Z. W. Chen, *Electrochim. Acta*, 247 (2017) 1103.
8. S. B. Xia, F. S. Li, X. Shen, X. Li, F. X. Cheng, C. K. Sun, H. Guo and J. J. Liu, *Mater. Lett*., 238 (2019) 171.
9. Y. L. Ding, J. Xie, G. S. Cao, T. J. Zhu, H. M. Yu and X. B. Zhao, *Adv. Funct. Mater*, 21 (2011) 348.
10. G.H. Waller, P.D. Brooke, B.H. Rainwater, S.Y. Lai, R. Hu, Y. Ding, F.M. Alamgir, K.H. Sandhage and M.L. Liu, *J. Power Sources*, 306 (2016) 162.
11. A. Tron, Y.D. Park and J. Mun, *J. Power Sources*, 325 (2016) 360.
12. H. Ming, Y. R. Yan, J. Ming, J. Adkins, X. W. Li, Q. Zhou and J. W. Zheng, *Electrochim. Acta*, 120

(2014) 390.
13. C. C. Zhang, X. Y. Liu, Q. L. Su, J. H. Wu, T. Huang and A. S. Yu, *ACS Sustainable Chem. Eng*., 5 (2017) 640.
14. Q. Wu, K. Xue, X. H. Zhang, X. S. Xie, H. Q. Wang, J. J. Zhang and Q. Y. Li, *Ceram. Int.*, 45 (2019) 5072.
15. Y. N. Zhang, Y. J. Zhang, M. Y. Zhang, M. L. Xu, X. Li, X. H. Yu and P. Dong, *JOM,* 71 (2019) 608.
16. H. Q. Liu, R. Y. Tian, Y. Jiang, X. H. Tan, J. K. Chen, L. N. Zhang, Y. J. Guo, H. F. Wang, L. F. Sun and W. G. Chu, *Electrochim. Acta*, 180 (2015) 138.
17. J. Lu, C. Zhan, T. P. Wu, J. G. Wen, Y. Lei, A. J. Kropf, H. M. Wu, D. J. Miller, J. W. Elam, Y. K. Sun, X. P. Qiu and K. Amine, *Nat. Commun*., 5 (2014) 5693.
18. H. Xia, Q. Y. Xia, B. H. Lin, J. W. Zhu, J. K. Seo and Y. S. Meng, *Nano Energy*, 22 (2016) 475.
19. P. Ram, R. Singhal, G. Choudhary and R. K. Sharma, *J. Electroanal. Chem*., 802 (2017) 94.
20. C. Y. Zhu, J. X. Liu, X. H. Yu, Y. N. Zhang, Y. J. Zhang, X. D. Jiang, S. Wang, Q. Wang and P. Dong, *J. Mater. Sci.: Mater. Electron*., 30 (2019) 5866.
21. Y. Fu, Y. J. Gu, Y. B. Chen, H. Q. Liu, Z. Z. Xu, W. L. Kong and Y. J. Wu, *Int. J. Electrochem. Sci*., 13 (2018) 8817.
22. L. Xiao, Y. L. Guo, D. Y. Qu, B. H. Deng, H. X. Liu and D. P. Tang, *J. Power Sources*, 225 (2013) 286.
23. X. D. Jiang, Z. T. Yuan, J. X. Liu, X. Jin, L. Y. Jin, P. Dong, Y. J. Zhang, Y. H. Yao, Q. Cheng, C. Liu, Y. N. Zhang and X. H. Yu, *Int. J. Electrochem. Sci.,* 13 (2018) 2341.
24. H. Q. Zhang, Q. J. Deng, C. X. Mou, Z. L. Huang, Y. Wang, A. J. Zhou and J. Z. Li, *J. Power Sources* 239 (2013) 538.
25. J. Guo, Y. X. Chen, C. R. Xu, Y. J. Li, S. Y. Deng, H. Xu and Q. Y. Su, *Ionics*, (2019) 1.
26. S. Zhao, Y. Bai, L. H. Ding, B. Wang and W. F. Zhang, *Solid State Ionics*, 247 (2013) 22.
27. M. Pasqualini, S. Calcaterra, F. Maroni, S.J. Rezvani, A. D. Cicco, S. Alexander, H. Rajantie, R. Tossici and F. Nobili, *Electrochim. Acta*, 258 (2017) 175.
28. Y. S. Shang, X. J. Lin, X. Lu, T. Huang and A. S. Yu, *Electrochim. Acta*, 156 (2015) 121.
29. S. B. Xia, F. S. Li, F. X. Cheng, X. Li, C. K. Sun, J. J. Liu and H. Guo, *J. Electrochem. Soc*., 165 (2018) A1019.
30. S. B. Xia, F. S. Li, F. X. Cheng and H. Guo, *J. Alloy. Compd*., 731 (2018) 428.
31. X. Y. Wang, H. Hao, J. L. Liu, T. Huang and A. S. Yu, *Electrochim. Acta*, 56 (2011) 4065.
32. F. Y. Lai, X. H. Zhang, H. Q. Wang, S. J. Hu, X. M. Wu, Q. Wu, Y. G. Huang, Z. Q. He and Q. Y. Li, *ACS Appl. Mater. Interfaces*, 8 (2016) 21656.